

Real-time spectral domain Doppler optical coherence tomography and investigation of human retinal vessel autoregulation

Bradley A. Bower

Mingtao Zhao

Duke University
Department of Biomedical Engineering
Durham, North Carolina 27708
E-mail: bradley.bower@duke.edu

Robert J. Zawadzki

University of California, Davis
Department of Ophthalmology and Vision Science
Sacramento, California 95817

Joseph A. Izatt

Duke University
Department of Biomedical Engineering
Durham, North Carolina 27708

Abstract. Investigation of the autoregulatory mechanism of human retinal perfusion is conducted with a real-time spectral domain Doppler optical coherence tomography (SDOCT) system. Volumetric, time-sequential, and Doppler flow imaging are performed in the inferior arcade region on normal healthy subjects breathing normal room air and 100% oxygen. The real-time Doppler SDOCT system displays fully processed, high-resolution [512 (axial) \times 1000 (lateral) pixels] *B* scans at 17 frames/sec in volumetric and time-sequential imaging modes, and also displays fully processed overlaid color Doppler flow images comprising 512 (axial) \times 500 (lateral) pixels at 6 frames/sec. Data acquired following 5 min of 100% oxygen inhalation is compared with that acquired 5 min postinhalation for four healthy subjects. The average vessel constriction across the population is $-16 \pm 26\%$ after oxygen inhalation with a dilation of $36 \pm 54\%$ after a return to room air. The flow decreases by $-6 \pm 20\%$ in response to oxygen and in turn increases by $21 \pm 28\%$ as flow returns to normal in response to room air. These trends are in agreement with those previously reported using laser Doppler velocimetry to study retinal vessel autoregulation. Doppler flow repeatability data are presented to address the high standard deviations in the measurements. © 2007 Society of Photo-Optical Instrumentation Engineers. [DOI: 10.1117/1.2772877]

Keywords: ophthalmology; Doppler effect; biomedical optics; laser Doppler velocimetry; real-time imaging; tomography.

Paper 06314SSR received Nov. 5, 2006; revised manuscript received Apr. 4, 2007; accepted for publication Apr. 19, 2007; published online Aug. 20, 2007. This paper is a revision of a paper presented at the SPIE Conference on Coherence Domain Optical Methods and Optical Coherence Tomography in Biomedicine X, Jan. 2006, San Jose, Calif. The paper presented there appears (unrefereed) in SPIE Proceedings Vol. 6079.

1 Introduction

Spectral domain optical coherence tomography (SDOCT) has been shown to be an excellent technique for imaging human retinal structure with high resolution and high speed *in vivo*.^{1,2} Doppler flow analysis using OCT has previously been successfully implemented in time-domain OCT systems^{3,4} for endoscopic⁵ and retinal flow⁶ characterization. Shortly after SDOCT was demonstrated in the retina, SDOCT-based implementations of Doppler and polarization-sensitive imaging were demonstrated for high-speed imaging of both flow velocity and birefringence in retinal tissue.⁷⁻⁹ The rapid development and application of these techniques to optophysiology are a burgeoning practice with potentially great importance for noninvasive characterization of retinal function.

OCT has been proven as a method for determining and tracking disease state in the retina. Time-domain OCT (TDOCT) has been used to examine conditions including age-related macular degeneration,¹⁰ macular edema,¹¹ and diabetic

retinopathy.¹² This technology has provided a new set of observables for studying pathology, including macular thickness, optic disk size, landmark (e.g., neovascular lesion) topography, and retinal vessel size. Perhaps less well studied is the use of functional OCT to study disease states. Doppler OCT has the potential to provide flow information to aid in the diagnosis or characterization of diseases affecting the retinal vasculature. Temporal observable changes, such as changes in thickness or flow rate, can also be used to characterize disease state.

Blood vessel autoregulation is the body's compensatory mechanism for adjusting blood flow in response to changes in gas partial pressures, notably oxygen and carbon dioxide, as well as intraocular pressure. Retinal autoregulation leads to vasoconstriction and decreased arterial flow rates in response to increased intraocular pressure or oxygen partial pressure. Doppler SDOCT can be used to directly determine the retinal flow and vessel diameter, and as such can be used to track the autoregulatory response over time.

Address all correspondence to Bradley Bower, Department of Biomedical Engineering, Duke University, 136 Hudson Hall-Box 90281, Durham, NC 27708; Tel: 919-660-2476; FAX: 919-613-9144; E-mail: bab15@duke.edu

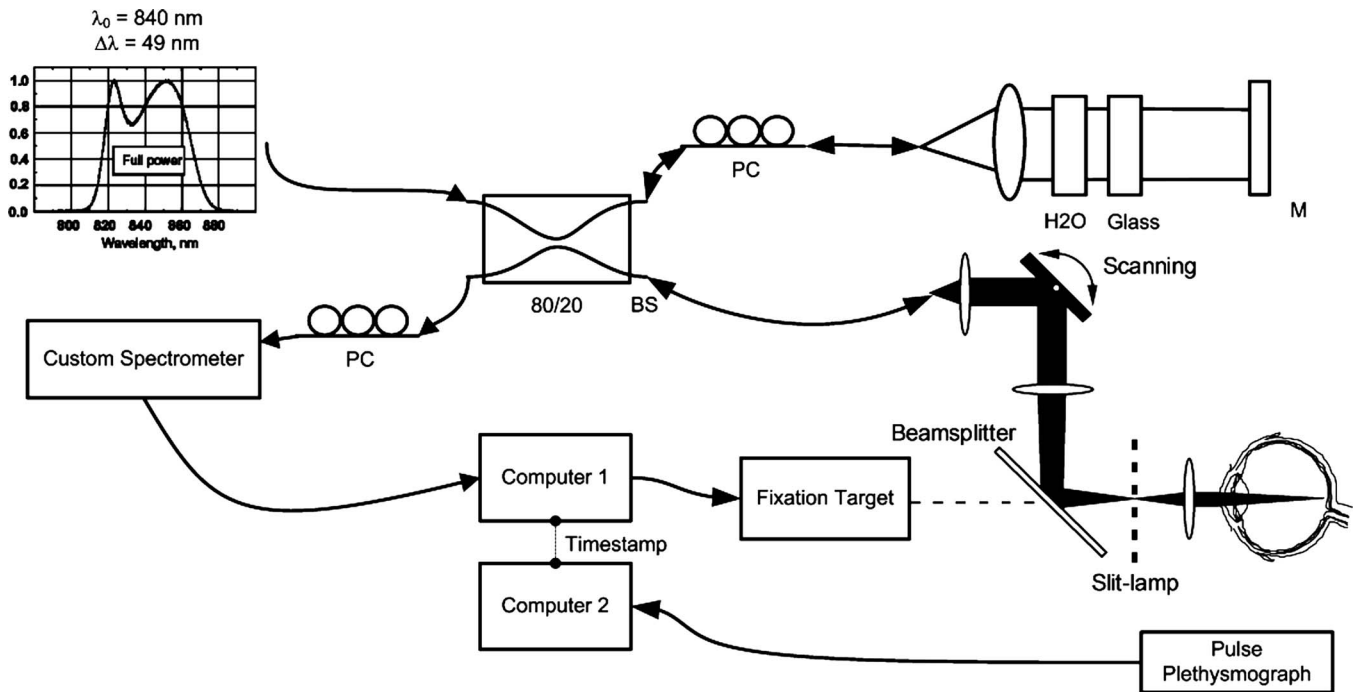


Fig. 1 Schematic for system for real-time SDOCT Doppler imaging. The system uses a source with a center wavelength of 840 nm and a bandwidth of 49 nm. Light is coupled to the sample and reference arms using an 80/20 fiber coupler, and the mixed light is detected with a custom high-speed, high-throughput spectrometer. The spectrometer detector consists of a 1024-pixel line-scan camera operated at a 20-kHz line rate. Two computers are used in this setup, one to control the SDOCT acquisition, processing, and display, and one to read in the plethysmograph data. The clocks on both computers are synchronized to atomic clock servers prior to acquisition and both the SDOCT frames and the plethysmograph data are time stamped to indicate the position in the cardiac cycle for each acquired frame.

The autoregulatory mechanism has been extensively studied using other techniques. Dumskyj et al.¹³ used laser Doppler velocimetry to probe retinal vessel flow. Intraocular pressure was increased via isometric exercise, and changes in flow and diameter were measured. An 8.4% rise in flow and 1.6% increase in vein diameter were measured with a 34% rise in venous perfusion pressure. A 4.8% rise in flow and 3.4% decrease in artery diameter were measured given a 33% rise in arterial perfusion pressure. Deutsch et al.¹⁴ used oxygen as a vasoconstrictor and measured vessel diameter changes using fluorescein angiography. After 100% oxygen inhalation, a $9 \pm 1\%$ decrease in artery diameter and a $15.9 \pm 1.4\%$ decrease in vein diameter were measured. Langhans, Michelson, and Groh¹⁵ used scanning laser doppler flowmetry to characterize the autoregulatory response in both normal subjects and smokers. Subjects inhaled 100% at 6 L/min for 5 min. While normals exhibited a 33% decrease in flow and a 26% decrease in flow volume, smokers only exhibited a 10% decrease in flow and a 12% decrease in flow volume, directly indicating an inhibited autoregulatory response. Finally, Kohnea, Patel, Rajjan, and Grunwald et al.^{16,17} used laser Doppler velocimetry to study the oxygen inhalation response in both normals and diabetics to gauge the affect of diabetic retinopathy on the autoregulatory mechanism. Grunwald et al. defined the oxygen reactivity metric as:

$$\%RO_2 = \frac{RBF_{\text{post}O_2}}{RBF_{\text{pre}O_2}} \cdot (100), \quad (1)$$

where $\%RO_2$ is the oxygen reactivity and RBF is retinal blood flow. The study found that normals had a $\%RO_2$ of

61%, whereas diabetics that did not present with retinopathy had a $\%RO_2$ of 53%. The most marked decrease was in diabetics with background retinopathy with a $\%RO_2$ of 38%, clearly indicating that diabetic retinopathy has a marked impact on retinal vessel autoregulation. As such, measuring retinal vessel autoregulation using Doppler SDOCT could potentially provide micron-scale, depth-dependent structural information supplemented by blood flow quantitation to support diagnosis of diabetic retinopathy.

2 Methods

We have developed a spectral domain Doppler optical coherence tomography (SDOCT) system that builds on previous work by using economical components and implementing rapid algorithms for real-time acquisition and display of volumetric, time-sequential, and Doppler flow image data. A schematic diagram of the real-time Doppler SDOCT system is illustrated in Fig. 1. The system uses a low-coherence superluminescent diode with a center wavelength of 841.9 nm and a bandwidth of 49 nm, yielding a theoretical full-width at half-maximum (FWHM) axial resolution of $7.5 \mu\text{m}$ in air and $5.4 \mu\text{m}$ in tissue. Lateral resolution is directly limited by the optics of the eye, and for the purpose of vessel diameter calculations is assumed to be $20 \mu\text{m}$. Sample arm light is delivered to the eye through a slit-lamp biomicroscope adapted for OCT with a scanning galvanometer pair and relay optics for live patient imaging. Reference and sample arm light interfere on a high-speed line camera at the output of a custom high-throughput spectrometer. Custom high-speed software (developed in collaboration with Bioptigen, Inc., Research Triangle

Park, North Carolina) is used for real-time data acquisition, processing, display, and archiving. For time-sequential B' -scan imaging, high-quality 512 (axial) \times 1000 (lateral) pixel B -scans at user-selectable retinal positions, and scan lengths are acquired and displayed at 17 frames/sec. The system sensitivity is defined by¹⁸:

$$\text{SNR} = \frac{P_s \cdot R \cdot \rho \cdot \tau}{2e}. \quad (2)$$

P_s is the power incident on the sample, R is the power reflectivity of the sample, ρ is the detector responsivity, τ is the integration time, and e is the electron charge constant. The maximum imaging depth z_{\max} is proportional to the spectral sampling interval $\delta_s k$ ¹⁸⁻²⁰:

$$z_{\max} = \frac{1}{4 \cdot \delta_s k}. \quad (3)$$

$\delta_s k$ is the wavenumber spacing at the detector plane, which is dependent on the spectral extent on the detector and the detector pixel spacing. The SDOCT signal is defined by the Fourier transform of the convolution of the interferometric data with the detector pixel shape. Thus a square pixel creates a sinc-shaped falloff function in sensitivity as a function of depth.^{21,22} The 3-dB falloff depth $z_{3\text{dB}}$ is limited by the optical resolution $\delta_s k$:

$$z_{3\text{dB}} = \frac{2 \ln 2}{\delta_s k}. \quad (4)$$

$\delta_s k$ is directly dependent on the grating used in the detection spectrometer.

For volumetric imaging, blocks of B -scan data acquired while raster scanning the OCT beam are acquired and used to construct "OCT fundus" images calculated from the maximum intensity axial projection of the volumetric datasets. OCT fundus images are also updated in real time as B -scan frames are acquired, with up to two fundus images/sec for 100×100 pixel raster volumes.^{23,24}

The signal processing steps implemented for real-time Doppler imaging are illustrated in Fig. 2. First, a user-adjustable number of SDOCT A scans are acquired at each transverse pixel position while B scanning. In common with amplitude imaging, the noninterferometric DC signal spectrum is estimated from the average of all A scans in each B scan, and subtracted from each A scan prior to further processing. A spectral rescaling approach² is used to correct for sample and reference arm dispersion mismatch before Fourier transformation of the data. The Doppler frequency f_D calculated for each image pixel, corresponding to the slope of the phase of SDOCT signal at each point in the image, is then estimated using the previously published algorithm²⁵:

$$f_D = \frac{\Delta\phi(z)}{2\pi T} = \frac{\arg \left\{ \frac{1}{N} \sum_{j=1}^N [f_{jT}(z) \cdot f_{(j+1)T}^*(z)] \right\}}{2\pi T}. \quad (5)$$

Here, $\Delta\phi(z)$ is the total change in phase and T is the total acquisition time required for N A scans to be acquired at each

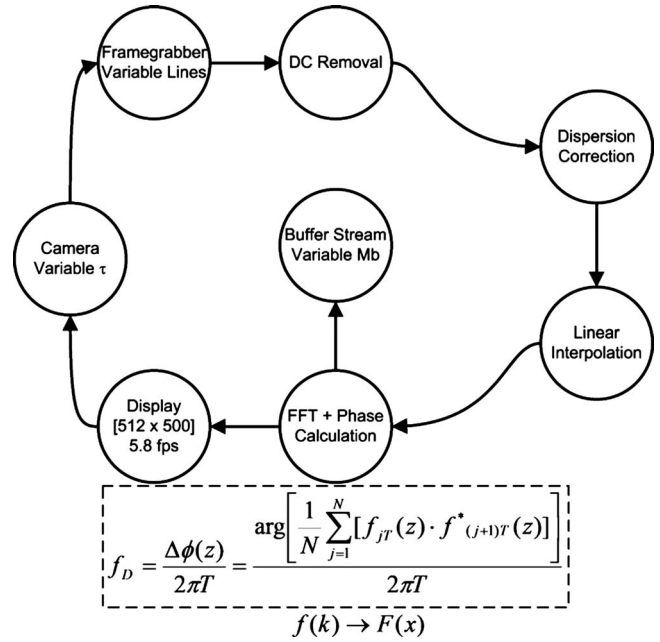


Fig. 2 Doppler SDOCT acquisition, processing, streaming, and display flow chart. DC removal is accomplished by summing across all A -scan lines, low-pass filtering the result, and subtracting the filtered A scan from all lines in the frame. Dispersion correction is accomplished using a spectral rescaling approach.² Linear interpolation transforms the spectral data from wavelength to wavenumber space. A Fourier transform translates the spatial frequency data to spatial position.

transverse pixel position, estimated from the summation in Eq. (5), where f_j represents an iteration over each A -scan line at each transverse pixel position. These data are used to generate 2-D Doppler frequency maps, which are color-coded, thresholded, and overlaid in real time on the grayscale B -scan data (1-D and 2-D Doppler flow profiles may also be extracted from saved datasets).

The minimum Doppler frequency that is detectable by this method is given by:^{7,8}

$$f_{\min} = \frac{\phi_{\text{noise}}}{2\pi T}, \quad (6)$$

where ϕ_{noise} represents the standard deviation of the phase in the absence of flow in the sample.²⁶ To measure ϕ_{noise} for our system, a stationary mirror was placed in a sample arm without galvanometric scanners, and the standard deviation of the phase recorded at the surface of the mirror over all A scans in a 500-line B scan was recorded. The phase noise is also affected by speckle noise and transverse motion, as indicated in Ref. 27. The maximum frequency that can be unambiguously detected is defined by:

$$f_{\max} = \frac{\phi_{\text{wrap}}}{2\pi T}, \quad (7)$$

where ϕ_{wrap} is π radians. For accumulated phase changes larger than $\pm\pi$ over the acquisition time T , the measured frequency wraps modulo 2π akin to other phase imaging techniques, and can potentially be unwrapped using standard

phase unwrapping techniques from phase microscopy. ϕ_{noise} is typically much lower in SDOCT systems compared to TDOCT systems, due primarily to the fixed reference arm. The dynamic range of Doppler frequencies in previous SDOCT systems has been shown to be as high as 600,⁷ which is at least a factor of 100 times that of TDOCT systems.^{28,29}

From the Doppler frequency data, flow velocity could in principle be determined by:

$$v = \frac{\Delta\phi \cdot \lambda_0}{4\pi \cdot T \cdot n \cdot \cos(\alpha)} = \frac{f_D \cdot \lambda_0}{2 \cdot n \cdot \cos(\alpha)}. \quad (8)$$

Here, λ_0 is the source center wavelength, n is the refractive index of the medium, and α is the angle of incidence of the probe beam relative to the moving scatterer. The angle of incidence is difficult to measure in retinal vessels, particularly in the arcades near the optic nerve head where they have significant axial curvature. As the relative change in flow and not the absolute flow velocity was necessary for this study, the Doppler angle was neglected and all values are reported in flow frequency.

For this study, four healthy subjects were imaged in accordance with the Declaration of Helsinki under Institutional Review Board approval. 100% oxygen was inhaled through a nonrebreather mask for 5 min with a flow rate of 6 L/min. Datasets were collected before inhalation of oxygen, following 5 min of pure oxygen inhalation, and following 5 min of recuperation post-oxygen inhalation. A finger-clip pulse plethysmograph (ADInstruments, Colorado Springs, Colorado) connected to a second computer was used to capture the cardiac cycle during SDOCT acquisition. Both the plethysmograph data and the SDOCT frames were time stamped, and the computer clocks were synchronized to the same atomic clock servers using a freely available utility (Chronos Atomic Clock Synchronizer, Chronos Atomic, www.chronosatomic.com) prior to acquisition. Fixation was maintained with a 280×220 color LCD panel in the visual field of the subject. An SDOCT aiming pattern consisting of alternating 10-mm horizontal and 10-mm vertical lines was raster scanned on the eye to determine alignment of the SDOCT scan through the pupil plane. A green cross on the fixation screen was collocated with the center of the aiming cross. The subject was first asked to focus on the center of the green cross, yielding an SDOCT scan of the fovea. After the foveal position was determined, the SDOCT scan was switched to acquire 1 mm, 100 lines per frame, 10 Doppler samples per line frames. This combination yields an imaging rate of 16 frames per sec, or about 6 sec per acquisition. Subject focus was then shifted nasally by moving the fixation cross until the SDOCT scan was approximately centered on the optic nerve head. The fixation cross was then moved to guide the subject focus such that the SDOCT image contained at least one of the vessels of the inferior arcade. Once this fixation position was established, a 10×10-mm SDOCT volumetric dataset was collected. The OCT fundus image created from this dataset was used to map the retinal vessel network and confirm patient fixation between time periods.

SDOCT Doppler frames were extracted and the time stamp on each frame was compared to the plethysmograph trace to ensure that the frames analyzed at all three time periods were collected during either a peak or trough in the trace. The Dop-

pler frame was then median filtered with a 3×3 kernel to remove salt and pepper noise. A Canny edge detector was then used to extract vessel edges. The edge pixel locations were then thresholded from the binary image and fed to an open-source ellipse-fitting routine.^{30,31} Retinal vessels acquired with SDOCT do not often appear circular due to a mismatch in the transverse and axial sampling. Also, raster scanning that is not parallel to the flow direction can create an angled slice through the vessels. To measure the true diameter of a vessel, it is then necessary to fit an ellipse to the vessel shape, extract the major and minor axes, and scale those values by the transverse and axial sampling to determine the true vessel diameter. The ellipse was then superimposed on the Doppler image for visual confirmation of the fit. Flow profiles along the major and minor axes were extracted using a quadratic polynomial fit. Vessel diameters were calculated as the major and minor axis lengths, scaled by the axial and lateral resolutions. The mean and standard deviation of the major and minor axis diameters were combined and reported as the vessel diameter statistics.

Data from one subject at four different time periods with no oxygen inhalation was also collected to determine repeatability between measurements. The same processing steps were applied to collect a table of Doppler repeatability data.

3 Results

Using Eq. (2), the predicted system sensitivity for 700 μW of power on the sample and 100- μs integration time is 110 dB. The sensitivity measured at 200 μm from the zero-pathlength difference location was 107 dB. For the purpose of the study, an integration time of 50 μs and an incident sample power of 380 μW was used, which leads to a theoretical sensitivity of 108 dB. The depth-dependent sensitivity falloff of the SDOCT system was about 15 dB over the entire imaging depth, as illustrated in Fig. 3. Following Eq. (3), the theoretical maximum depth is 2.25 mm while the measured maximum depth occurred at 2.2 mm. The 3-dB falloff point [Eq. (4)] is calculated to occur at 1.3 mm and was found at 1.0 mm from the zero-pathlength difference location. For the settings given, the minimum Doppler frequency calculated from the measured phase noise standard deviation using Eq. (6) was 51 Hz, or 0.016 radians. The maximum frequency before phase wrapping [Eq. (7)] for 50- μs integration time is 5 kHz. The Doppler frequency dynamic range was thus approximately 100, or 40 dB. System performance results are summarized in Table 1.

Figure 4 includes a wide-angle (2.2×12 mm) SDOCT B scan of one subject as well as a single frame from the real-time color Doppler image of the selected artery/vein pair imaged for the purpose of this study. Figure 5 shows the processing steps undergone to extract the vessel diameter and peak flow data. Tables 2 and 3 detail the results of the repeatability measurements. Table 2 lists the data from all four trials, while Table 3 indicates the repeatability error, as defined by the measurements standard deviation divided by the mean. The study results, including mean and standard deviation values for both peak flow and vessel diameter, are indicated in Table 4.

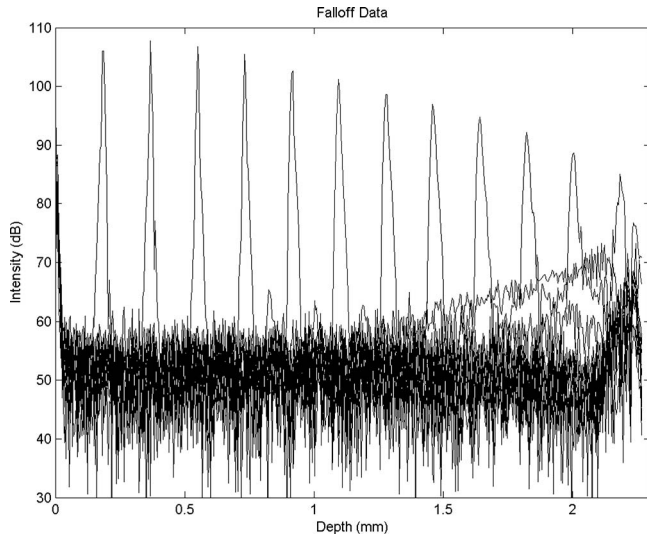


Fig. 3 Measured SDOCT system sensitivity as a function of depth. The theoretical system sensitivity at zero pathlength difference is 110 dB for an integration time of 100 μ s. Depth-dependent sensitivity falloff is dependent on detector pixel size and is complicated by dispersion mismatch between the reference and sample arms. Spectral rescaling was used to correct for dispersion mismatch, yielding a depth-dependent sensitivity falloff of about 15 dB over the entire imaging depth. The 3-dB falloff point is theoretically 1.3 mm and was experimentally measured to occur at 1.0 mm.

4 Discussion

The mean diameter change in response to increased blood oxygenation was -16% , indicating vasoconstriction, and the diameter change after a return to room air was 36% , indicating vasodilation, as expected. The mean flow change after 100% oxygen was -6% , and after the relaxation period it was

Table 1 SDOCT system performance data. Theoretical and measured axial resolution values are for air/tissue. The theoretical value for Doppler frequency minimum is not available, as this value is dependent on the phase stability of the system. The maximum frequency limit was not confirmed directly for this study, but depends only on the A-scan repetition rate which was confirmed by monitoring the line scan camera frame trigger signal.

Parameter	Theoretical	Measured
Axial resolution	6.38 μ m/ 4.56 μ m	7.5 μ m/ 5.36 μ m
SNR ($\tau=100 \mu$ s)	110 dB	107 dB at 200 μ m
z_{max}	2.25 mm	2.2 mm
$z_{3 \text{ dB}}$	1.3 mm	1.0 mm
f_{min}	N/A	51 Hz
f_{max}	5 kHz	N/A
Doppler dynamic range	40 dB	N/A

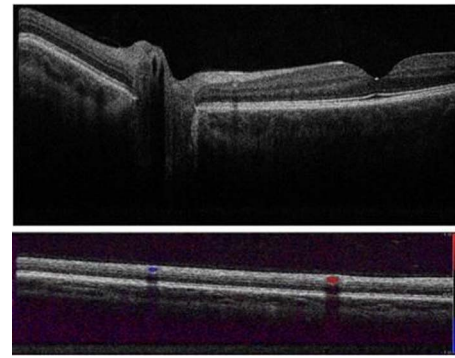


Fig. 4 Top: wide-angle 2.2 (axial) \times 15 mm (lateral) SDOCT B-scan comprising 512 (axial) \times 1000 (lateral) pixels along the papillomacular axis in a normal human retina acquired, processed, and displayed at a real-time rate of 17 frames/sec. Bottom: overlaid color Doppler signal from OD retinal vessels in the same subject. Scan location is nasal and superior to optic disk. 512 \times 500 Doppler frequency images of 2.2 mm (axial) \times 6 mm (lateral) were acquired at 5.8 frames per sec with six lines acquired at each lateral position for Doppler processing.

21%. These trends are consistent with those reported previously in that the effect of increased partial pressure of oxygen prompts vasoconstriction and the autoregulatory mechanism causes a vasodilation after a rest period with normal room air inhalation. The standard deviations, though, are high, with $\pm 26\%$ at vasoconstriction and $\pm 54\%$ at vasodilation for the vessel diameter and ± 20 and $\pm 28\%$ for the flow at vasoconstriction and dilation, respectively. Repeatability data indicated in Tables 2 and 3 shed some light on this problem. Repeatability, defined as the standard deviation of the measurement for all four trials divided by the mean for all four trials, indicates the tolerances for the Doppler autoregulation measurements. The major axis diameter repeatability was 12.4%, the minor axis repeatability was 10.1%, and the peak flow repeatability was 30.8%, indicating that at least that much variability can be expected in Doppler measurements. It should be noted, however, that while the repeatability values are on the order of the changes expected due to oxygen inhalation (9 to 16% decrease in vessel diameter and 30% decrease in flow), the group response from all four subjects still indicates the ability to distinguish the gross effects of oxygen inhalation.

Repeatability data were collected on one subject across four time periods with no physiological change induced between measurements. Fixation was held constant and the only change was the position and angle of the subject's head relative to the scanning beam. This indicates that patient head positioning can have an affect on Doppler and structural measurements, and it calls into question the ability to accurately acquire Doppler data as part of a longitudinal study. A more thorough analysis of imaging angle and its effect on measured values, however, is beyond the scope of this study.

Doppler SDOCT may have significant advantages over commercially available laser Doppler flowmeters. The Heidelberg Retina Flowmeter (HRF, Heidelberg Engineering, Inc., Vista, California) has been extensively used in clinical retinal research.³²⁻³⁷ Specifications for the HRF include a 10- μ m transverse and 300- μ m longitudinal resolution. 256 \times 64

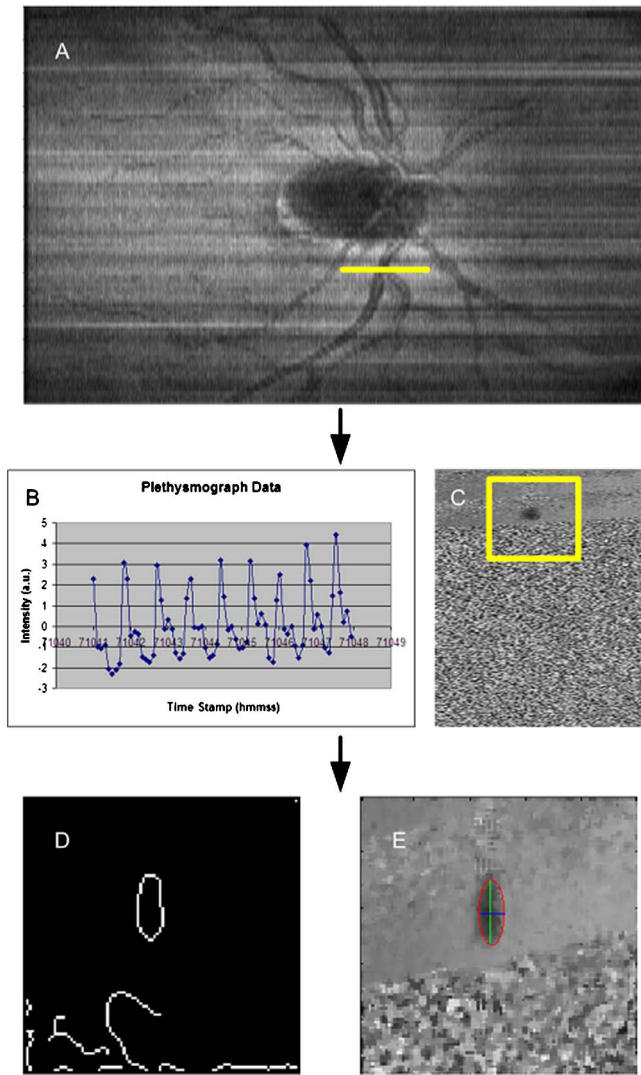


Fig. 5 Processing steps to measure the diameter and peak flow from Doppler data. (a) Representative OCT fundus image showing the relative location of vessel data in the inferior arcades. (b) Plethysmograph data are used to correlate the acquired Doppler data with the cardiac cycle, and a frame of SDOCT data, corresponding to either a peak or trough in the plethysmograph plot, is used for all three study periods. The time stamp is given in hhmmss, where h is hours (on a 12-hour clock), m is minutes, and s is seconds. A subset of the image [yellow box in (c)] is extracted for analysis. 3×3 median filtering and Canny edge detection (d) are used to create an edge map of the vessel borders. An ellipse is fit to the edges (e) and the diameter is calculated from the lengths of the major and minor axes and scaled by the lateral and axial resolutions. Peak flow is found as the maximum of a parabolic fit to profiles along the major and minor axes.

blood flow maps are acquired in 2 sec with additional time needed for processing. Doppler SDOCT processing is performed in real time, which provides the operator with Doppler B scans of vessels quickly enough to observe pulsatile flow as it occurs. With further development, Doppler SDOCT could play an important role in performing real-time flow measurements of the retinal vasculature.

Grunwald et al.¹⁷ demonstrated the use of laser Doppler flowmetry in the study of retinal vascular disease, specifically detailing impaired changes in blood flow due to a decreased

Table 2 Repeatability data. A vessel in the inferior arcade was located by adjusting the patient fixation while acquiring Doppler data. The fixation position was then fixed and the subject was asked to sit back from the slit lamp between Doppler measurements. MDiam (m) is the diameter in meters as measured along the major axis of an elliptical fit to the vessel in question. mDiam is the diameter in meters along the minor axis. Peak flow is the maximum value from a parabolic fit to the flow profiles along the major and minor axes. If the two profiles had different peak flow values, the maximum value was used.

Align	MDiam (m)	mDiam (m)	Peak flow
1	9.85E-05	1.40E-04	3.13E+04
2	8.34E-05	1.80E-04	3.11E+04
3	7.65E-05	1.60E-04	3.28E+04
4	7.65E-05	1.60E-04	1.49E+04
Mean	8.3725E-05	0.00016008	2.75E+04
Standard deviation	1.0373E-05	1.6208E-05	8.46E+03

autoregulatory response in subjects with diabetic retinopathy. Given the marked improvements exhibited by Doppler SDOCT over conventional laser Doppler flowmetry and the recent commercial availability of a Doppler SDOCT imaging system (Bioptigen, Inc.), Doppler SDOCT may have increased utility for studying diseases of the retinal vasculature.

Future studies would benefit greatly from three improvements: bulk motion frequency correction, eye tracking, and improved angular alignment. Gross patient motion induces subtle low-frequency shifts across the data, and while data for this study were selected based on the absence of bulk motion artifacts, the presence of a bulk motion frequency correction algorithm such as that proposed by White et al.⁷ would allow for imaging subjects who are not good fixators or are unable to remain stationary over the course of the acquisition. An eye tracking system³⁸ would greatly aid in repeatable vessel landmark location and B-scan alignment. It is postulated that the repeatability data indicate the need for more accurate angular alignment of the probe beam relative to the retina, as subtle shifts in the angle may distort both the diameter and flow measurements.

This study illustrates that real-time Doppler SDOCT, using an internal fixation target for vessel identification and positioning, is sufficient for single-vessel flow analysis. Repeat-

Table 3 Repeatability data results. Repeatability error is defined as the standard deviation across all four trials listed in Table 2, divided by the mean value from all trials. These values indicate the tolerances expected for any Doppler SDOCT measurements.

Value	Repeatability error
Major diameter	12.39%
Minor diameter	10.13%
Peak flow	30.76%

Table 4 Study data. Property indicates the measurand while time refers to the time period in question. 1->2 indicates the change between no oxygen and breathing oxygen for 5 min 2->3 relates the change between having inhaled oxygen for 5 min and breathing room air for another 5 min. The diameter data are the average of the major and minor axis diameter data.

Property	Time	Change
Mean Diameter change	1->2	-15.57%
	2->3	36.47%
Std Diameter change	1->2	26.23%
	2->3	53.81%
Mean Peak Flow change	1->2	-6.19%
	2->3	20.60%
Std Peak Flow change	1->2	20.00%
	2->3	27.58%

ability errors in Doppler measurements raise questions as to the use of Doppler SDOCT in longitudinal studies, but as has been demonstrated, Doppler SDOCT is capable of measuring trends in flow and diameter changes and can be used to track physiological changes initiated by the autoregulatory mechanism.

Acknowledgments

The authors wish to acknowledge Yimin Wang for assistance in performing the phase stability measurement and Zhilin Hu for optical design of the high-throughput spectrometer. The authors also acknowledge Eric Buckland and Bennett Gros-hong of Bioptigen, Inc. (Research Triangle Park, North Carolina) for collaboration in the development and provision of real-time Doppler SDOCT software, which is now commercially available. This work was supported by NIH grants EB000243, RR019769, EY013516, and EY014743.

References

1. N. A. Nassif, B. Cense, B. H. Park, M. C. Pierce, S. H. Yun, B. E. Bouma, G. J. Tearney, T. C. Chen, and J. F. de Boer, "In vivo high-resolution video-rate spectral-domain optical coherence tomography of the human retina and optic nerve," *Opt. Express* **12**(3), 367-376 (2004).
2. M. Wojtkowski, V. J. Srinivasan, T. H. Ko, J. G. Fujimoto, A. Kowalczyk, and J. S. Duker, "Ultrahigh-resolution, high-speed, Fourier domain optical coherence tomography and methods for dispersion compensation," *Opt. Express* **12**(11), 2404-2422 (2004).
3. Z. Chen, T. E. Milner, S. Srinivas, X. Wang, A. Malekafzali, M. J. C. v. Gemert, and J. S. Nelson, "Noninvasive imaging of *in vivo* blood flow velocity using optical Doppler tomography," *Opt. Lett.* **22**, 1119-1121 (1997).

4. J. A. Izatt, M. D. Kulkarni, S. Yazdanfar, J. K. Barton, and A. J. Welch, "In vivo bidirectional color doppler flow imaging of picoliter blood volumes using optical coherence tomography," *Opt. Lett.* **22**(18), 1439-1441 (1997).
5. V. X. D. Yang, M. L. Gordon, S. J. Tang, N. E. Marcon, G. Gardiner, B. Qi, S. Bisland, E. Seng-Yue, S. Lo, J. Pekar, B. C. Wilson, and I. A. Vitkin, "High speed, wide velocity dynamic range Doppler optical coherence tomography (Part 3): *in vivo* endoscopic imaging of blood flow in the rat and human gastrointestinal tracts," *Opt. Express* **11**(19), 2416-2424 (2003).
6. S. Yazdanfar, A. M. Rollins, and J. A. Izatt, "In vivo imaging of human retinal flow dynamics by color {Doppler} optical coherence tomography," *Arch. Ophthalmol. (Chicago)* **121**, 235-239 (2003).
7. B. R. White, M. C. Pierce, N. Nassif, B. Cense, B. H. Park, G. J. Tearney, B. E. Bouma, T. C. Chen, and J. F. de Boer, "In vivo dynamic human retinal blood flow imaging using ultra-high-speed spectral domain optical Doppler tomography," *Opt. Express* **11**(25), 3490-3497 (2003).
8. R. A. Leitgeb, L. Schmetterer, W. Drexler, A. F. Fercher, R. J. Zawadzki, and T. Bajraszewski, "Real-time assessment of retinal blood flow with ultrafast acquisition by color Doppler Fourier domain optical coherence tomography," *Opt. Express* **11**(23), 3116-3121 (2003).
9. R. Leitgeb, L. F. Schmetterer, M. Wojtkowski, C. K. Hitzenberger, M. Sticker, and A. F. Fercher, "Flow velocity measurements by frequency domain short coherence interferometry," *Proc. SPIE* **4619**, 16-21 (2002).
10. M. R. Hee, C. R. Baumal, C. A. Puliafito, J. S. Duker, E. Reichel, J. R. Wilkins, J. G. Coker, J. S. Schuman, E. A. Swanson, and J. G. Fujimoto, "Optical coherence tomography of age-related macular degeneration and choroidal neovascularization," *Ophthalmology* **103**(8), 1260-1270 (1996).
11. M. R. Hee, C. A. Puliafito, C. Wong, J. S. Duker, E. Reichel, B. Rutledge, J. S. Schuman, E. A. Swanson, and J. G. Fujimoto, "Quantitative assessment of macular edema with optical coherence tomography," *Arch. Ophthalmol. (Chicago)* **113**(8), 1019-1029 (1995).
12. W. Goebel and T. Kretzchmar-Gross, "Retinal thickness in diabetic retinopathy—a study using optical coherence tomography (OCT)," *Retina J. Retinal Vitreous Diseases* **22**(6), 759-767 (2002).
13. M. J. Dumskyj, J. E. Eriksen, C. J. Dore, and E. M. Kohner, "Autoregulation in the human retinal circulation: assessment using isometric exercise, laser Doppler velocimetry, and computer-assisted image analysis," *Microvasc. Res.* **51**, 378-392 (1996).
14. T. A. Deutsch, J. S. Read, J. T. Ernest, and T. K. Goldstick, "Effects of oxygen and carbon dioxide on the retinal vasculature in humans," *Arch. Ophthalmol. (Chicago)* **101**, 1278-1280 (1983).
15. M. Langhans, G. Michelson, and M. J. M. Groh, "Effect of breathing 100% oxygen on retinal and optic nerve head capillary blood flow in smokers and non-smokers," *Br. J. Ophthalmol.* pp. 365-369 (1997).
16. E. M. Kohner, V. Patel, and S. M. B. Rassam, "Role of blood-flow and impaired autoregulation in the pathogenesis of diabetic retinopathy," *Diabetes* **44**(6), 603-607 (1995).
17. J. E. Grunwald, C. E. Riva, A. J. Brucker, S. H. Sinclair, and B. L. Petrig, "Altered retinal vascular-response to 100-percent oxygen breathing in diabetes-mellitus," *Ophthalmology* **91**(12), 1447-1452 (1984).
18. M. A. Choma, M. V. Sarunic, C. H. Yang, and J. A. Izatt, "Sensitivity advantage of swept source and Fourier domain optical coherence tomography," *Opt. Express* **11**(18), 2183-2189 (2003).
19. A. F. Fercher, C. K. Hitzenberger, G. Kamp, and S. Y. Elzaiat, "Measurement of intraocular distances by backscattering spectral interferometry," *Opt. Commun.* **117**(43), 183-188 (1995).
20. G. Hausler and M. W. Lindner, "Coherence radar and spectral radar—new tools for dermatological diagnosis," *J. Biomed. Opt.* **3**, 21 (1998).
21. S. H. Yun, G. J. Tearney, B. E. Bouma, B. H. Park, and J. F. de Boer, "High-speed spectral-domain optical coherence tomography at 1.3 μm wavelength," *Opt. Express* **11**(26), 3598-3604 (2003).
22. R. Leitgeb, C. K. Hitzenberger, and A. F. Fercher, "Performance of Fourier domain vs. time domain optical coherence tomography," *Opt. Express* **11**(8), 889-894 (2003).
23. A. G. Podoleanu, J. A. Rogers, and D. A. Jackson, "OCT *en face* images from the retina with adjustable depth resolution in real time," *IEEE J. Sel. Top. Quantum Electron.* **5**(4), 1176-1184 (1999).

24. S. L. Jiao, R. Knighton, X. R. Huang, G. Gregori, and C. A. Puliafito, "Simultaneous acquisition of sectional and fundus ophthalmic images with spectral-domain optical coherence tomography," *Opt. Express* **13**(2), 444–452 (2005).
25. L. Wang, Y. Wang, S. Guo, J. Zhang, M. Bachman, G. P. Li, and Z. Chen, "Frequency domain phase-resolved optical Doppler and Doppler variance tomography," *Opt. Commun.* **242**, 345–350 (2004).
26. M. A. Choma, A. K. Ellerbee, S. Yazdanfar, and J. A. Izatt, "Doppler flow imaging of cytoplasmic streaming using spectral domain phase microscopy," *J. Biomed. Opt.* **11**(2), 024014 (2006).
27. B. H. Park, M. C. Pierce, B. Cense, and J. F. de Boer, "Real-time multi-functional optical coherence tomography," *Opt. Express* **11**(7), 782–793 (2003).
28. A. M. Rollins, S. Yazdanfar, J. K. Barton, and J. A. Izatt, "Real-time *in vivo* color Doppler optical coherence tomography," (submitted for publication).
29. S. Yazdanfar, M. D. Kulkarni, and J. A. Izatt, "High resolution imaging of *in vivo* cardiac dynamics using color Doppler optical coherence tomography," *Opt. Express* **1**(13), 424–431 (1997).
30. R. Halir and J. Flusser, "Numerically stable direct least squares fitting of ellipses," *Proc. Intl. Conf. Central Europe Computer Graphics, Visual. Interactive Digital Media*, pp. 125–132 (1998).
31. D. Hanselman, "Stable direct least squares ellipse fit," Matlab Central File Exchange, Matlab, Inc., Natick, MA (2005).
32. J. Ludovico, R. Bernardes, I. Pires, J. Figueira, C. Lobo, and J. Cunha-Vaz, "Alterations of retinal capillary blood flow in preclinical retinopathy in subjects with type 2 diabetes," *Graefe's Arch. Clin. Exp. Ophthalmol.* **241**(3), 181–186 (2003).
33. R. K. Ghanta, A. Harris, E. Hertzmark, H. Pakter, J. Simpson, V. R. F. Guedes, W. Drexler, J. G. Fujimoto, L. Kagemann, and J. S. Schuman, "Evaluation of retinal blood flow using the Heidelberg Retina Flowmeter and nerve fiber layer thickness using optical coherence tomography in a glaucomatous monkey model," *Invest. Ophthalmol. Visual Sci.* **42**(4), S15–S15 (2001).
34. M. H. M. Cuypers, J. S. Kasanardjo, and B. C. P. Polak, "Retinal blood flow changes in diabetic retinopathy measured with the Heidelberg scanning laser Doppler flowmeter," *Graefe's Arch. Clin. Exp. Ophthalmol.* **238**(12), 935–941 (2000).
35. G. Michelson, B. Schmauss, M. J. Langhans, J. Harazny, and M. J. M. Groh, "Principle, validity, and reliability of scanning laser Doppler flowmetry," *J. Glaucoma* **5**(2), 99–105 (1996).
36. P. Lundmark, M. Rawji, J. Flanagan, and G. Trope, "Variability of blood flow measurements using the Heidelberg retinal flowmeter," *Invest. Ophthalmol. Visual Sci.* **37**(3), 1215–1215 (1996).
37. H. Chen, C. Hudson, S. Ataullah, and D. McLeod, "The acute effect of smoking on retinal blood flow: An assessment with the Heidelberg retina flowmeter," *Invest. Ophthalmol. Visual Sci.* **37**(3), 1237–1237 (1996).
38. D. X. Hammer, R. D. Ferguson, J. C. Magill, L. A. Paunescu, S. Beaton, H. Ishikawa, G. Wollstein, and J. S. Schuman, "Active retinal tracker for clinical optical coherence tomography systems," *J. Biomed. Opt.* **10**(2), 024038 (2005).